

# On Transferability of Machine Learning Force Fields: A Case Study on Silicon

Howard Yanson,<sup>1,2</sup> David Zagaceta,<sup>1</sup> Brandon C. Wood,<sup>2</sup> and Qiang Zhu<sup>1,\*</sup>

<sup>1</sup>*Department of Physics and Astronomy, University of Nevada, Las Vegas, NV 89154, USA*

<sup>2</sup>*Materials Science Division, Lawrence Livermore National Laboratory, Livermore, California 94550, USA*

(Dated: July 4, 2022)

In this article, we present a systematic study in developing machine learning interatomic potential (MLIAP) for elemental silicon. Previously, many of MLIAP applications involve fitting models to small or localized training sets, which do not allow for transferability. The need for transferability of MLIAP is crucial in sampling the vast phase space in the application of crystal structure prediction. To address for this need, we indicate that two primary factors can have major influences on the transferability of the MLIAP. First, transferability depends strongly on the diversity of the training data set. In particular, the use of a random structures generating algorithm based on crystal symmetry is a suitable methodology for generating a training data set with sufficient diversity. Second, we introduce a framework that allows Gaussian symmetry functions and bispectrum coefficients descriptors to be fitted with generalized linear regression or neural network. According to our substantial benchmark, the best accuracy trained on the diverse data set can be achieved by using a flexible machine learning method coupled with highly orthogonal descriptors. Therefore, we will show that neural network potential fitting with bispectrum coefficients as the descriptor is a feasible method for obtaining high-quality and transferable MLIAP.

## I. INTRODUCTION

Atomistic modeling methods such as molecular dynamics (MD) or Monte Carlo (MC) play important roles in investigating time-dependent physical and chemical processes. In these methods, energy and forces need to be recalculated iteratively as the atomic configurations evolve. Consequently, atomistic simulations crucially depend on the accuracy of the underlying potential energy surface (PES). Modern quantum mechanical modeling based on density functional theory (DFT) can consistently generate accurate energetic descriptions for many solid systems<sup>1</sup>. However, MD simulations based on DFT suffer from the highly demanding computational cost. The simulations are only suitable to model a system with up to a few thousands of atoms at tens of picoseconds. On the other hand, classical force field (FF) method is widely employed to simulate materials with up to millions of atoms at a large timescale (hundreds of nanoseconds). This method has enabled many explorations that lead to revealing interesting physical and chemical phenomena<sup>2-4</sup>. However, the construction of a reliable PES of classical FF method remains problematic. In developing classical FF, a set of parameters are fitted to a few DFT and/or experimental data to compute the potential energy of a system given an analytic functional form. Due to the constraints on the functional form and the limitation of training data set, the accuracy of classical FF is not dependable.

Meanwhile, *in-silico* materials discovery requires an accurate yet efficient energy model to screen materials' properties in high-throughput manner. In the past decade, the discoveries of new materials have been highly driven by advanced structure prediction methods such as crystal structure prediction (CSP)<sup>5</sup> and data mining<sup>6</sup>. In both cases, DFT method is used to perform geometry relaxation and energy evaluation. Despite the power of the current supercomputer, the computational cost for DFT simulation is still a bottleneck to many important and fascinating puzzles in materials science. Ideally, an approach that preserves DFT accuracy without sacrificing

the computational cost is desirable.

To resolve the limitations described above, many efforts have been devoted towards establishing machine learning based interatomic potential (MLIAP) method. Compared to the DFT method, MLIAP approach demands far lower computational cost (2-4 orders of magnitude lower) while retaining accuracy at the DFT level. The power of MLIAP method is illustrated by many applications to a range of materials<sup>7-10</sup>. A large amount of DFT data (structures, energy, forces, and stresses) are required to develop an accurate MLIAP. The structures must be represented by appropriate descriptors (high-dimensional real valued array) in order to identify the similarities and/or dissimilarities in the atomic environments. In MLIAP fitting, a variety of regression techniques are used to correlate between the descriptor and energy/forces. Several machine learning techniques for developing MLIAP had been successfully implemented: linear/polynomial regression<sup>11-14</sup>, Gaussian process regression<sup>15,16</sup>, and high-dimensional neural network potential (NNP)<sup>17,18</sup>. A benchmark study of these machine learning methods were recently inspected for the performance and cost to many elemental systems<sup>19</sup>. Nevertheless, many of the published MLIAPs do not have transferability which is crucial in crystal structure prediction.

In the past few years, researchers attempted to combine the MLIAP generation with crystal structure prediction<sup>10,20-23</sup>. For example, Hajinazar *et al.* employed a structure prediction technique to generate diverse data sets than the common but less diverse data set generated with MD-based approach. The diverse data sets of multi-component system were used to develop NNPs<sup>20</sup>. Furthermore, it was proposed that the generation of MLIAPs could be performed in conjunction with structure prediction processes. The active learning approach in constructing a MLIAP on-the-fly was employed automatically to deal with extrapolation outside the training domain. Then, the MLIAP replaced the DFT gradually for structural relaxation and energy evaluation with much lower computational cost. Active learning technique had been successfully applied to predict PES reconstructions of several challenging

elemental systems<sup>22,23</sup> and multi-component system<sup>21</sup>.

In this report, we will discuss about our attempts in developing accurate and transferable MLIAP for elemental silicon as the prototypical system. Many silicon MLIAPs had been developed using the training data sets obtained by running MD simulations and selecting known structural prototypes manually<sup>10,15,19,24–28</sup>. These configurations from MD trajectories tend to possess strong correlations with the initial geometry. Hence, the resulting MLIAPs can only describe a few energy basins of the entire PES, i.e. low transferability. We believe that there are two main factors can influence the transferability of the MLIAP. First, training data set generated with high-throughput structure prediction method can enhance the transferability. Here, we generate a diverse silicon data set by using our in-house code, PyXtal<sup>29</sup>—a Python package for random crystal structure generation. The DFT-quality data set spans a large space in the PES covering many energy basins, and the DFT setting is provided in section II A. Second, we enable a machine learning infrastructure that allows Gaussian symmetry functions and bispectrum coefficients descriptors to be trained with generalized linear regression and neural network. The details of the descriptors and the regression techniques are available in section II B and section II C, respectively. Finally, we will systematically construct NNP with bispectrum coefficients, due to the high orthogonality, as the descriptors in section III.

## II. COMPUTATIONAL METHODOLOGIES

### A. *Ab initio* calculation

*Ab initio* calculations are necessary to provide the training data set for MLIAP development. In this study, we employed PyXtal<sup>29</sup> software to generate several thousands of structural configurations. For each configuration, the total energy and forces were calculated at DFT level through the ASE package<sup>30</sup>. ASE provides interface to the VASP code<sup>31</sup> within projector augmented wave methodology<sup>32</sup> to perform geometry relaxations. In our calculation, we used the PBE-GGA<sup>33</sup> as the exchange-correlation functional with an energy cutoff of 600 eV and a  $\Gamma$ -centered KSPACING of 0.15.

### B. Descriptors

Descriptors, as the unique numerical representations of atomic structures, play an essential part in constructing MLIAP. It is crucial for a descriptor to be able to distinguish the local environments of atomic structures. While the most common choice of representation by atomic coordinates is convenient, but it poorly describes the structural environments. The Cartesian coordinates of a crystal structure can change through translational or rotational operation, while the energy remains invariant. Thus, physically meaningful descriptors must be unaffected by these alterations to the structural environment, and any permutation of atoms should not change the descriptors. Additionally, the descriptors must be

continuously differentiable within the domain of local atomic environment. In the last decade, the atom-centered descriptors, which probe the atomic environment by its neighboring vectors, become popular because they fit the criteria. The descriptors usually operate within a cutoff function to ensure that the descriptors smoothly vanish to zero at a given cutoff radius,  $R_c$ . A popular cutoff function choice is the so called cosine cutoff function. The function is expressed in the following:

$$f_c(R_{ij}; R_c) = \begin{cases} \frac{1}{2} \left[ \cos\left(\frac{\pi R_{ij}}{R_c}\right) + 1 \right] & R_{ij} \leq R_c \\ 0 & \text{otherwise} \end{cases} \quad (1)$$

where  $R_{ij}$  is the distance between the center atom  $i$  and the neighbor atom  $j$ .

Among the atom-centered descriptors, Gaussian symmetry function<sup>17</sup> and bispectrum coefficients<sup>15</sup> are widely used in the materials modelling community. Their definitions will be discussed briefly as follows.

#### 1. Gaussian Symmetry Functions

Gaussian symmetry functions are used regularly to represent the local atomic environments of crystal structures in NNP development. Commonly used Gaussian symmetry functions are two-body ( $G^2$ ) and three-body ( $G^4$ ) symmetry functions:

$$G_i^2 = \sum_{j \neq i} e^{-\eta(R_{ij}-R_s)^2} f_c(R_{ij}) \quad (2)$$

$$G_i^4 = 2^{1-\zeta} \sum_{j \neq i} \sum_{k \neq i, j} (1 + \lambda \cos \theta_{ijk})^\zeta \cdot e^{-\eta(R_{ij}^2 + R_{ik}^2 + R_{jk}^2)} \cdot f_c(R_{ij}) \cdot f_c(R_{ik}) \cdot f_c(R_{jk}) \quad (3)$$

$G^2$  is mainly designed to capture the radial environment while  $G^4$  is used for describing the angular part by including the three-body  $ijk$  terms.  $R_s$  shifts the center of the Gaussian functions to a certain radius resulting in spherical shell with the Gaussian width of  $\eta$ .  $\zeta$  controls the angular resolution, and  $\lambda$  usually takes the value of +1 and -1 for inverting the cosine function. The cutoff function ( $f_c$ ) is consistent with Eq. 1. There is a set of  $G_i^2$  and  $G_i^4$  descriptors specifying the center atom  $i$  in relation to the neighboring atoms  $j$  in terms of radial and angular parts. For a real material system, this set of parameters need to be optimized by a more extensive search<sup>34–37</sup>.

#### 2. Bispectrum Coefficients

Similar to Gaussian symmetry functions, SO(4) bispectrum can be used to represent the local atomic environments. It was first introduced by Bartók *et al.* for the training of machine learning FF (MLFF) on the elemental systems of Group

IVA<sup>15</sup>. A detailed study of SO(4) bispectrum as a descriptor along with several alternative implementations (SO(3) bispectrum, angular Fourier series, and SOAP kernel) is available in Ref.<sup>24</sup>. Later, Thompson *et al.* proposed the spectral neighbor analysis method (SNAP) method and demonstrated that the SO(4) bispectrum could achieve satisfactory accuracy based on the simple linear<sup>11</sup> and quadratic regressions<sup>12</sup>. Following the original work, the expression of SO(4) bispectrum is formed by the expansion coefficients of 4D hyperspherical harmonics:

$$B_i^{l_1, l_2, l} = \sum_{m, m' = -l}^l (c_{m', m}^l)^* \sum_{m_1, m'_1 = -l_1}^{l_1} \sum_{m_2, m'_2 = -l_2}^{l_2} c_{m'_1, m_1}^{l_1} c_{m'_2, m_2}^{l_2} H_{l_1, m_1, m'_1, l_2, m_2, m'_2}^{l, m, m'} \quad (4)$$

where  $H_{m'_1, m'_2, m', m_1, m_2, m}^{l_1, l_2, l}$  is the analog to the Clebsch-Gordan coefficients on the 3-sphere. In application, it is the product of two ordinary Clebsch-Gordan coefficients on the 2-sphere.  $c_{l_1, m_1, l_2, m_2}^{l, m}$  are the expansion coefficients from the hyperspherical harmonics ( $U_{m', m}^l$ ) functions that are projected from the atomic neighborhood density within a cutoff radius onto the surface of four-dimensional sphere:

$$\rho = \sum_{l=0}^{+\infty} \sum_{m=-l}^{+l} \sum_{m'=-l}^{+l} c_{m', m}^l U_{m', m}^l \quad (5)$$

where the expansion coefficients are defined as

$$c_{m', m}^l = \langle U_{m', m}^l | \rho \rangle \quad (6)$$

In this work, our implementation of SO(4) bispectrum or bispectrum descriptor is very similar to the SNAP method<sup>11</sup> that is implemented in the LAMMPS code<sup>38</sup>. However, we introduce another method to calculate the hyperspherical harmonics and their gradients<sup>39</sup>. The benefit of this method is that it allows for the removal of singularities at the north and south poles of the 3-sphere that exist in the traditional implementation. Furthermore, we also include an option to normalize the expansion coefficients from the hyperspherical harmonics, where the normalization factor is  $\frac{\sqrt{2l+1}}{4\pi}$ . The impacts of normalization on the MLFF training will be discussed later in section III C.

### C. Machine Learning Force Field Fitting

The construction of the total energy ( $E_{\text{total}}$ ) of a structure can be obtained by the summation of atomic energy ( $E_i$ ) evaluated from atom-centered descriptors,  $\mathbf{X}_i$ :

$$E_{\text{total}} = \sum_i^{\text{all atoms}} E_i(\mathbf{X}_i) \quad (7)$$

The atomic energy contributions depend on the local structural environment within a cutoff radius with respect to the center

atom  $i$ . Furthermore, accurate representation of PES is also dependent on the contributions of forces. The force acted on atom  $j$  can be expressed by the negative gradient of the energy with respect to its atomic positions ( $\mathbf{r}_j$ ):

$$\mathbf{F}_j = - \sum_i^{\text{all atoms}} \frac{\partial E_i(\mathbf{X}_{ij})}{\partial \mathbf{X}_{ij}} \cdot \frac{\partial \mathbf{X}_{ij}}{\partial \mathbf{r}_j} \quad (8)$$

The functional forms of  $E$  and  $F$  are fully dependent on the regression algorithm. Generalized linear regression and neural network (NN) regression will be discussed in the following sections.

#### 1. Generalized Linear Regression

Linear regression is the most fundamental approach in curve fitting. In this context, each atomic energy is assumed to be linearly correlated with the descriptors. Thus, the total energy can be expressed as follows,

$$E_{\text{total}} = \beta_0 + \beta \cdot \sum_{i=1}^N \mathbf{X}_i, \quad (9)$$

where  $\beta_0$  and  $\beta$  are the weights presented in scalar and vector forms, and  $N$  is the total atoms in a structure.

In general, the total energy can be described as a generalized linear regression with extended polynomial terms. Below is a version to the second-order (quadratic) expansion in the Taylor series:

$$E_{\text{total}} = \beta_0 + \beta \cdot \sum_{i=1}^N \mathbf{X}_i + \frac{1}{2} \sum_{i=1}^N \mathbf{X}_i^T \cdot \mathbf{A} \cdot \mathbf{X}_i \quad (10)$$

where  $\mathbf{A}$  is the symmetric weight matrix (i.e.  $\mathbf{A}_{12} = \mathbf{A}_{21}$ ) describing the quadratic terms. From linear to quadratic regression, the size of weight coefficients increases from  $N + 1$  to  $(N+1)(N+2)/2$ . Indeed, the energy can be further expanded to higher order. However, we restrict it to the second-order expansion due to the drastic increase in the size of weight coefficients.

Correspondingly, the force of an atom  $j$  can be expressed in this form by expanding the terms in Eq. 8 with Eq. 10:

$$\mathbf{F}_j = \sum_{i=1}^N \left( -\beta \cdot \frac{\partial \mathbf{X}_i}{\partial \mathbf{r}_j} - \frac{1}{2} \left[ \frac{\partial \mathbf{X}_i^T}{\partial \mathbf{r}_j} \cdot \mathbf{A} \cdot \mathbf{X}_i + \mathbf{X}_i^T \cdot \mathbf{A} \cdot \frac{\partial \mathbf{X}_i}{\partial \mathbf{r}_j} \right] \right) \quad (11)$$

Both energy and force terms have a linear correlation with the expanded descriptors through a set of weight coefficients  $\{\beta_0, \beta_1, \dots, \beta_N, \mathbf{A}_{11}, \mathbf{A}_{12}, \dots, \mathbf{A}_{NN}\}$ . For convenience, we call the set of coefficients as  $\mathbf{w}$  from now on. To obtain the best  $\mathbf{w}$ , we solve the objective cost function following the least squares formula for both energy and force,

$$\Delta = \frac{1}{2s} \sum_{i=1}^s \left[ \left( \frac{E_i - E_i^{\text{Ref}}}{N_{\text{atom}}^i} \right)^2 + \frac{\beta}{3N_{\text{atom}}^i} \sum_{j=1}^{3N_{\text{atom}}^i} (F_{i,j} - F_{i,j}^{\text{Ref}})^2 \right] \quad (12)$$

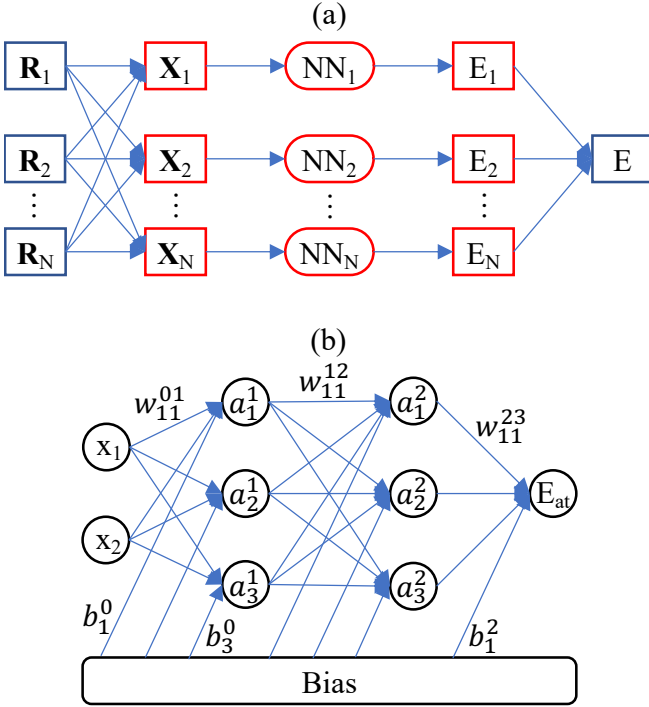


FIG. 1. (a) A schematic diagram of high-dimensional neural network. The red-colored diagrams are parts of (b) the neural network architecture. Each atom in a structure is firstly mapped into atom-centered descriptors according to the atomic environment of the structure. The atom-centered descriptors serve as the inputs in the neural network architecture that outputs the atomic energy. Finally, the collection of the atomic energies is the total energy of the structure.

where  $s$  is the total number of structures,  $i$  loops over all structures, and  $j$  loops over all atoms for each structure  $i$  in all three directions.  $N_i^{\text{atom}}$  is the total number of atoms in the structure  $i$ . Here,  $\beta$  is acting as the balance parameters, as the number of force components is much larger than the number of energies. The cost function compares the predicted values obtained from the regression ( $E_i$  and  $F_{i,j}$ ) to the true values of  $E^{\text{Ref}}$  and  $F_{i,j}^{\text{Ref}}$ . Then, the optimum solution can be solved by finding the  $w$  leading to the zero partial derivative of  $\Delta$  with respect to each element in  $w$ . In this study, we used the *numpy.linalg.lstsq*<sup>40</sup> solver for linear regression problem.

## 2. Neural Network Regression

In this section, the high-dimensional NN (Fig. 1) is introduced. The regression based on NN can be considered as an extension of linear regression model. For a crystal structure that consists of  $N$  atoms, there are  $N$  positions ( $R_N$ ) for the atoms to arrange themselves.  $N$  atom-centered descriptors ( $X_i$ ) for the structure can be mapped based on this atomic configuration. Each of the atom-centered descriptors is, then, fed into a NN architecture (Fig. 1b). NN architecture consists of input, hidden, and output neurons. These neurons are or-

ganized in layers as shown. The neurons in the first layer (input layer) are occupied by the atom-centered descriptors. The neuron at the output layer defines the atomic energy,  $E_i$ . Hidden layers lie between the input and output layers. In the case of Fig. 1b, there are two hidden layers. In particular, we will call this NN architecture, 2-3-3. 2 represents two neurons in the input layers. 3-3 represents two hidden layers with 3 neurons each. The output layer of the NN architecture is always 1. Therefore, it is redundant to be mentioned. The neurons in hidden layers represent no physical meaning. They act as a functional form to predict the atomic energy. There is no limit to the number of hidden layers. However, the flexibility of NNP will depend on the number of neurons present in the NN architecture. The connectivity in between the neurons are the weight parameters (fitting parameters). Mathematically, one can calculate the value of a neuron in this form:

$$X_{n_i}^l = a_{n_i}^l \left( b_{n_i}^{l-1} + \sum_{n_j=1}^N W_{n_j, n_i}^{l-1, l} \cdot X_{n_j}^{l-1} \right) \quad (13)$$

The value of a neuron ( $X_{n_i}^l$ ) at layer  $l$  can be determined by the relationships between the weights ( $W_{n_j, n_i}^{l-1, l}$ ), the bias ( $b_{n_i}^{l-1}$ ), and all neurons from the previous layer ( $X_{n_j}^{l-1}$ ).  $W_{n_j, n_i}^{l-1, l}$  specifies the connectivity of neuron  $n_j$  at layer  $l-1$  to the neuron  $n_i$  at layer  $l$ .  $b_{n_i}^{l-1}$  represents the bias of the previous layer that belongs to the neuron  $n_i$ . These connectivity are summed based on the total number of neurons ( $N$ ) at layer  $l-1$ . Finally, an activation function ( $a_{n_i}^l$ ) is applied to the summation to induce non-linearity to the neuron ( $X_{n_i}^l$ ).  $X_{n_i}$  at the output layer is equivalent to an atomic energy, and it represents an atom-centered descriptor at the input layer. Since the atomic energy has no reference value to the DFT energy, each atomic energy is collected as in Eq. 7 to obtain the total energy of a crystal structure. The accuracy of NNP will rely on the accuracy of the NN architecture to predict the energy.

To train the NNP, we can consistently use the cost function in Eq. 12. To prevent overfitting, it is useful to add a penalty term to account for the complexity of the entire weights ( $m$ ) to the Eq. 12,

$$\Delta_p = \frac{\alpha}{2s} \sum_{i=1}^m (w^i)^2 \quad (14)$$

where  $\alpha$  is a dimensionless number that controls the degree of penalty. Adding such penalty function in the context of machine learning is called regularization. To solve this minimization problem, we developed in-house stochastic gradient decent and ADAM<sup>41</sup> optimizer. Alternatively, we interfaced our in-house code with the Scipy package<sup>42</sup>, so it is possible to use the L-BFGS method<sup>43</sup> for this study.

## III. RESULTS

In this section, we discuss about the development of accurate and transferable MLIAP. First, we introduce two types of data sets—a localized data set and a diverse data set. Second, we will validate our machine learning framework with



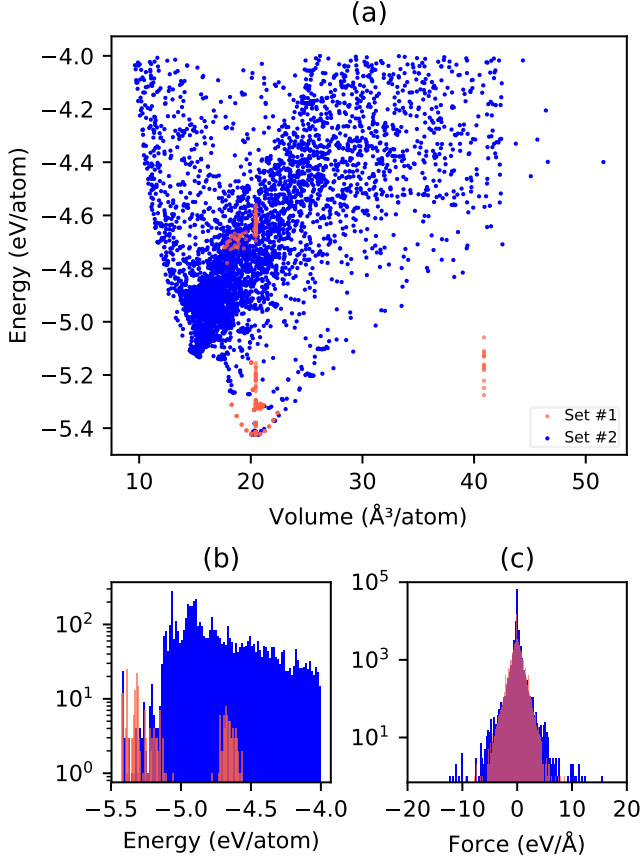


FIG. 2. (a) The energy versus volume plot for training Set #1 and Set #2. The histograms of energy and forces are presented in (b) and (c), respectively.

the localized data set as the baseline. Third, we explore the interplay between bispectrum coefficients and the two machine learning regressions (generalized linear regression and NN) on the localized data set. This subsection is dedicated to further validate the localized data set with a new NNP fitting strategy. Finally, we will develop a transferable silicon MLIAP based on the new strategy.

### A. Training Data Sets

Here, we present two silicon data sets. The first set (Set #1) is the localized data set, obtained from Ref.<sup>19</sup>. Set #1 contains 244 structures in total (219 for training and 25 for test), which includes the ground state of crystalline structure, strained structures, slabs, and configurations from MD simulations. To generate the diverse data set, we utilized our in-house PyXtal code<sup>29</sup> to produce thousands of silicon structures with various numbers of atoms in the unit cell from 2, 4, 6, 8 to 16. Random space group (1 to 230) assignment was applied to these silicon structures. For each random structure, we performed four consecutive geometry optimization steps at the level of DFT with steady increase in precision. The maximum numbers for each ionic step were 10, 25, 50 and

TABLE I. The setting used to compute the atom-centered descriptors in this study. The Gaussian symmetry functions are consistent with Ref.<sup>19</sup>, except that  $R_c$  was set to 4.8  $\text{\AA}$  for the quadratic regression in the previous literature. Moreover, we considered bispectrum coefficients with the band limit  $l_{\max}$  up to 8. The asterisk symbol denotes the reduced parameter set for Gaussian symmetry functions.

Descriptors	Parameters	Values
$G^2$	$R_c$ ( $\text{\AA}$ )	5.2
	$R_s$ ( $\text{\AA}$ )	0
	$\eta$ ( $\text{\AA}^{-2}$ )	0.036*, 0.071*, 0.179*, 0.357*, 0.714*, 1.786*, 3.571, 7.142, 17.855
$G^4$	$R_c$ ( $\text{\AA}$ )	5.2
	$\lambda$ ( $\text{\AA}$ )	-1, 1
	$\zeta$	1
	$\eta$ ( $\text{\AA}^{-2}$ )	0.036*, 0.071*, 0.179*, 0.357*, 0.714, 1.786, 3.571, 7.142, 17.855
$B$	$R_c$ ( $\text{\AA}$ )	4.9
	$l_{\max}$	2, 3, 4, 5, 6, 7, 8
	Normalization	True, False

50. The relaxed images were then selected to our training pool to represent the shape of PES towards the energy minima. Afterwards, we performed single-point DFT calculations for all configurations in the training pool using the parameters described in section II A. Finally, 5352 silicon structures (Set #2) were selected by removing structures with energies that are higher than -4.0 eV/atom. In total, Set #1 has 15078 atoms, and Set #2 has 31004 atoms. We note that the energy cutoff (600 eV) used in our DFT calculation is slightly higher than the one (520 eV) used in Ref.<sup>19</sup>. However, this resulted in negligible differences according to our test for the same structures. Therefore, we will use these two data sets for direct comparison in the following sections.

As shown in Fig. 2, Set #2 covers more diverse atomic environments in terms of energy, force, and density. Set #1 includes 244 structures that span from -4.560 to -5.425 eV/atom in energy, and 17.56 to 40.89  $\text{\AA}^3/\text{atom}$  in density. The energy of Set #2 ranges from -4.0 to -5.425 eV/atom, and the density ranges from 8.295 to 52.81  $\text{\AA}^3/\text{atom}$ . Moreover, the force distribution in Set #2 is clearly wider than that in Set #1. As we will show in the following, a more diverse set is beneficial to obtain a better machine learning force field (MLFF) for more general purposes, especially in constructing PES for CSP purpose.

All structures in two data sets were used to compute the Gaussian symmetry functions as mentioned in Section II B. For consistency purposes, we employed the same parameter setting as reported in Ref.<sup>19</sup>, which is summarized in Table I. In the original literature, there were 9  $G^2$  and 18  $G^4$  descriptors. We made a deeper inspection on the histogram of the computed Gaussian symmetry functions from the entire Set #1. We identified that descriptors with large  $\eta$  values span in a very narrow range. The narrow-range descriptors were less likely to discriminate different local atomic environments, and they may introduce numerical noise. Therefore, we reduced the parameter sets, which included only 6  $G^2$  and 8  $G^4$  descriptors for this study. The reduced parameter sets are

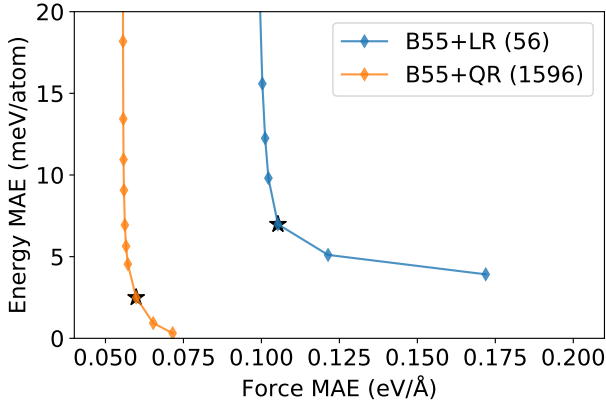


FIG. 3. The comparison of fitting between linear and quadratic regression based on the B55 descriptors ( $l_{\max} = 4$ ) applied to Set #1. For each regression, the energy MAE and force MAE values were collected by gradually varying the force coefficients from  $1e-6$  to 1. The numbers of weight parameters are given in the parentheses. The marked black asterisks correspond the results when the force coefficient is at  $1e-4$ .

marked with asterisk symbol. For convenience, we are naming the full Gaussian symmetry functions as G27 and the reduced Gaussian symmetry functions as G14. For the bispectrum coefficients, similar to Fourier series, the expansion is exact as long as  $l_{\max}$  goes to infinity. However, this will generate infinite bispectrum coefficients and require infinite computations. Since the higher indices of  $l$  can only be beneficial in detecting subtle signals on the neighbor density map, the expansion of the bispectrum coefficients is limited to several finite orders. In this study, we only considered the band limit ( $l_{\max}$ ) up to 8. However, we mainly focused on three values (3, 4, and 5), which have 30, 55, and 90 bispectrum coefficients, respectively. They are denoted as B30, B55, and B91. Furthermore, we investigated the case of  $B$  with normalization, and they are denoted as  $\hat{B}30$ ,  $\hat{B}55$ , and  $\hat{B}91$ .

### B. Validation with the Localized Data Set

In Ref.<sup>19</sup>, the authors presented an extensive benchmark for silicon (as well as several other elemental systems) with different MLFF approaches. This provided us a foundation to validate our MLFF implementations. With Set #1, we attempted to reproduce the results based on the NNP, SNAP, and quadratic SNAP (qSNAP) methods. They corresponded to the NN regression with G27 descriptors (NNP+G27), linear regression with B55 descriptors (LR+B55), and quadratic regression with B55 descriptors (QR+B55). For the cases of linear and quadratic regressions, the results are deterministic as long as the force coefficient in Eq. 12 is given. Fig. 3 displays the gradual changes of mean absolute error (MAE) values for energy and forces by varying the force coefficient ( $\beta$ ) from  $1e-6$  to 1 for both LR+B55 and QR+B55. For each regression, these points seem to form a Pareto front. Namely, there is no single point which can beat the other points in both energy and force MAE values. Here, we choose a range from

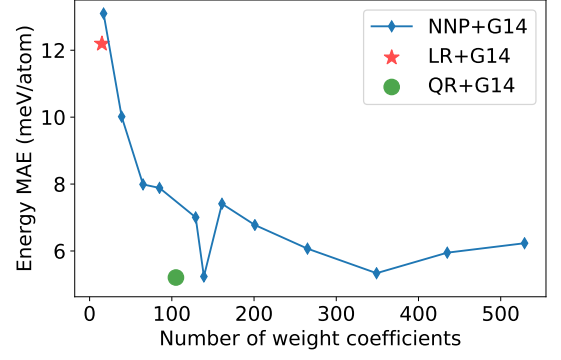


FIG. 4. The performance of NN regression on G14 as a function of hidden layer sizes of [1], [4], [8], [2, 2], [4, 4], [6, 6], [8, 4], [8, 8], [12, 6], [12, 12], [14, 14], and [16, 16]. For comparison, the results from linear and quadratic regressions are also included.

the Pareto front which leads to an approximately even change on other sides. This point corresponds to the force coefficient closest to  $1e-4$ . When  $\beta = 1e-4$ , B55+LR yields the MAE values of 6.94 (6.28) meV/atom for energy and 0.11 (0.12) eV/Å for force in training (test) data set. For B55+QR, the results gain significant improvement. The final energy MAE value is 2.50 (2.21) meV/atom, and the force MAE value is 0.06 (0.08) eV/Å. The results are expected since the quadratic form allows the coupling of bispectrum coefficients<sup>12</sup>. However, the number of weight parameters also increases notably from 56 to 1596, which increases the computational cost for both FF training and prediction.

For NNP+G27, we tested the NNP fitting with NN architecture of 27-24-24. The predicted MAE values are 5.65 meV/atom in the training data set and 5.60 meV/atom in the test data set. The metrics are close to the previously reported values: 5.88 and 5.60 meV/atom in Ref.<sup>19</sup>. Our force MAE values are 0.095 and 0.106 eV/Å, agreeing with the previous report as well. Furthermore, we employed reduced Gaussian descriptors to the NNP fitting (NNP+G14). We found that the training with NNP+G14 also yielded comparable metrics. This indicated that the removed Gaussian descriptors were indeed redundant, and they can cause numerical noise during the NNP training. Correspondingly, we adjusted our NNP training strategy toward G14 to investigate the impacts of hyperpa-

TABLE II. The comparison of mean absolute error (MAE) values between this work and Ref.<sup>19</sup> for the same 244 Si data set (Set #1). The results from Ref.<sup>19</sup> are shown in parentheses. For LR+B55 and QR+B55, the results are shown when force coefficient is at  $1e-4$ . For the NNP fitting, we used the NN architectures of 27-24-24 and 14-12-12.

Fitting Method	Train Energy (meV/atom)	Test Energy (meV/atom)	Train Force (eV/Å)	Test Force (eV/Å)
LR+B55	6.94 (6.38)	6.28 (6.89)	0.11 (0.21)	0.12 (0.22)
QR+B55	2.50 (3.98)	2.21 (3.81)	0.06 (0.18)	0.08 (0.17)
NNP+G27	5.65 (5.88)	5.60 (5.60)	0.09 (0.12)	0.11 (0.11)
NNP+G14	5.95	6.33	0.10	0.11

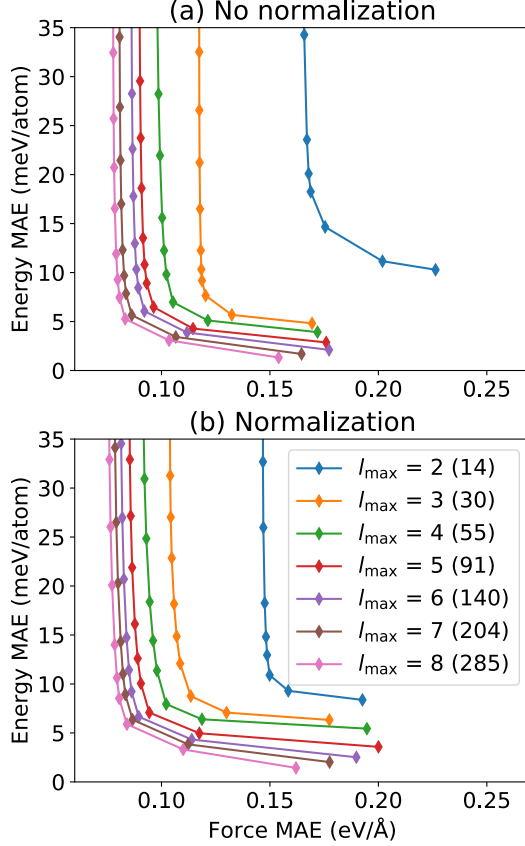


FIG. 5. The performance of linear regression based on the bispectrum coefficients without (a) and with normalization (b). In each plot,  $l_{\max}$  values from 2 to 8 were considered. The number of descriptors are given in the parenthesis.

rameters on NNP training. In contrast to linear regression, the NNP training is invulnerable to the choice of force coefficient since the NNP can compromise for more flexible functional forms. It is rather reliant to the hidden layer size. Fig. 4 shows the energy MAE values scanning across the hidden layer sizes for NNP+G14 with  $\beta$  fixed at 0.03. Overall picture suggests that NNP performances tend to improve as the NNP model becomes more flexible. However, the NNP accuracy will saturate at some point. Beyond the saturation point, increasing the hidden layer size will only raise the computational cost and lower the chance of finding optimal weight parameters.

The results with different training strategies are summarized in Table II. Compared to Ref.<sup>19</sup>, our results are close or maybe slightly better. Therefore, we proceed to make further investigations on Set #1 by using different strategies.

### C. Bispectrum Coefficients/Algorithms Interplay

In this section, MLFF fitting with bispectrum coefficients will be discussed in details by using both generalized linear and NN regressions on Set #1. First, the performances of gen-

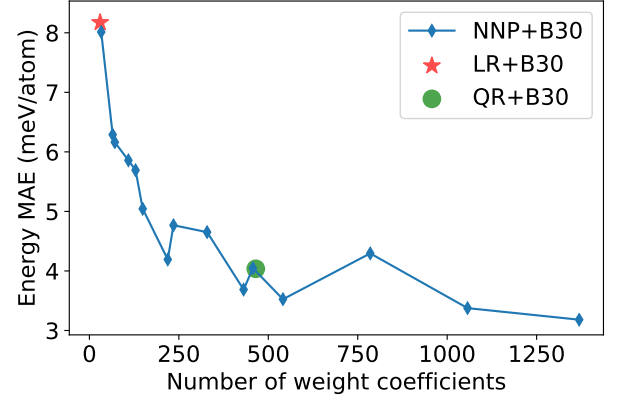


FIG. 6. The performance of NN regression on B30 applied to Set #1 as a function of hidden layer size. The following hidden layer sizes were used: [1], [2], [4], [2, 2], [4, 4], [6, 4], [6, 6], [8, 8], [10, 10], [12, 6], [12, 12], [16, 16], [24, 12], and [24, 24]. For comparison, the results from linear and quadratic regressions are also included

eralized linear regression can be improved based on the normalization factor of bispectrum coefficients prior to the MLFF fitting. In the original implementation of SNAP<sup>11</sup>, the bispectrum coefficients are not normalized prior to the MLFF fitting. However, Fig. 5 shows the benefits of normalization prior to the MLFF fitting. Linear regression achieves better performances for both energy and forces as  $l_{\max}$  increases. At  $l_{\max} > 5$ , there are no significant gains in the MAE values as the computational cost increases. The insignificance of normalization can be due to the limitation of linear regression ability to express the complexity.

Second, Fig. 6 shows the NNP fitting with bispectrum coefficients as the inputs to the neural network architecture. The results of NNP+B30 are trained with different hidden layer sizes. The best accuracy is achieved with the hidden layer size of [24, 24]. The 30-24-24 architecture includes 1369 descriptors in total. The training MAE values are 3.18 meV/atom and 0.07 eV/Å, and the test MAE values are 3.54 meV/atom and 0.08 eV/Å. These metrics reach comparable values to that from QR+B55 (see Table II) with less bispectrum coefficients. For reference, linear regression and quadratic regression results are marked in Fig. 6. Clearly, NNP with bispectrum coefficients gain notable improvements in comparison to linear regression and quadratic regression. The improvements are expected since NN allows more flexible functional forms to describe the deviation from linearity. Meanwhile, quadratic regression gives better accuracy due to the extended polynomial forms. However, it is possible to attain similar accuracy in NNP fitting with smaller number of weights.

### D. Training with More Diverse Data Set

From computational perspective, NNP fitting with Gaussian symmetry functions expends less cost than with bispectrum coefficients. However, bispectrum coefficients cover more orthogonal set and are easier to be expanded. The results

of the bispectrum coefficients clearly show the superiority in descriptors. In addition, it is more time consuming to search for optimal solution in NNP training than QR fitting in general. However, applying the trained NNP to predict for new structures yields the same time complexity as the LR and QR models. Predominantly, NNP with bispectrum coefficients is assumed to provide better model with a larger number of descriptors and training samples, as it allows flexible MLIAP fitting.

Thus far, we have discussed different training strategies applied to Set #1. Our in-house code has the ability to apply various descriptors and regression techniques to train MLIAP with satisfactory accuracy ( $< 10$  meV/atom in energy MAE and  $0.15$  eV/Å in force MAE). Using the MLIAP trained on Set #1, we tried to validate the prediction power on Set #2 (the more diverse data set). The prediction power of the MLIAP on Set #2 is extremely poor. It is not surprisingly as the machine learning ability in extrapolation is known to be poor. The performance of the MLIAP yields great accuracy based on the given training data set. The characteristic atomic environment of Set #2 is too broad and most of the data points are not present in the training of Set #1. Therefore, the predicted energy and force are no longer reliable.

To train reliable MLIAP on Set #2, we decided to use more bispectrum coefficients and a larger NN architecture and make Set #1 as the test data set. Fig. 7 shows the accuracy of NNP+B30, NNP+B55, and NNP+B91 with different NN architecture. Clearly, the NNP performance tends to increase as more descriptors and more weights are added. In term of energy, the MLIAP on Set #2 gives reasonable MAE values on the test set. This suggests that the MLFF with diverse data set possess transferability. However, the force MAE values on the test set are consistently larger than the train set. This can indicate that Set #1 contains some atomic configurations from manual selection. These manually selected configurations contain some atomic environments which are not fully covered by our random generated structures. The best accuracy obtained in this study is by using 91-28-28 architecture. However, 91-28-28 architecture does not predict the test set as well as the train set. For optimum choice, 55-32-16 architecture provides the best balance accuracy and precision between the train and test sets in term of energy.

In comparison, the previously reported study<sup>24</sup> for diverse silicon clusters gave comparable results. In the study, the authors juxtaposed several different descriptors in depth. The descriptors are coupled with Gaussian process regression—non-parametric regression—algorithm for MLIAP development. The errors of MLIAP with bispectrum coefficients are reported in root mean square error (RMSE). The RMSE for energy and forces with  $l_{\max}$  at 8 are  $22.8$  eV/atom and  $0.26$  eV/Å, respectively. At  $l_{\max} = 10$ , the RMSE values are  $20.2$  eV/atom and  $0.25$  eV/Å. Correspondingly, our MLIAP on Set #2 with 55-32-16 architecture gives the RMSE values of  $21.6$  eV/atom and  $0.18$  eV/Å. Moreover, the RMSE values with 91-28-28 architecture give  $19.8$  eV/atom and  $0.15$  eV/Å. The differences in the results, especially in the force training, can be due to that Set #2 is more diversified, and NNP allows flexible fitting.

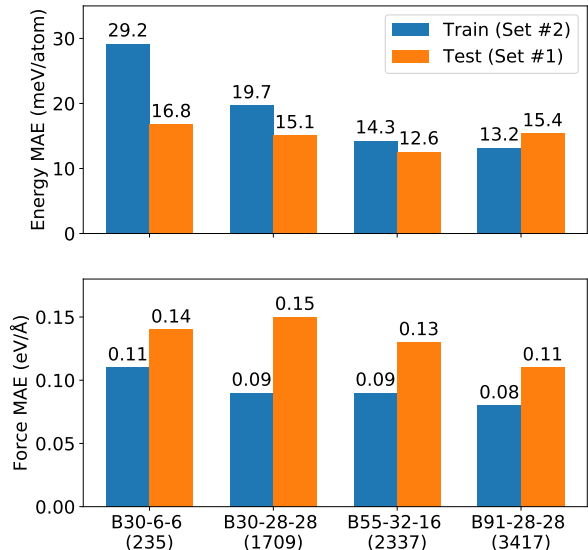


FIG. 7. The performance of trained MLIAP on Set #2.

#### IV. DISCUSSION

*Training data set.* In general, MLFF lacks extrapolative ability, unlike the traditional force field method. The training data set plays an extremely important role in MLFF development. A more complete data set can grant the trained MLFF with more powerful predictive ability. The use of randomly pre-symmetrized crystal structures is able to produce a data set with highly diverse atomic distribution<sup>22,29,44</sup>. In addition, DFT calculations only provide the total energy for each atomic configuration, and the NNP is trained to describe the total energy of a structure. However, it is possible that the NNP fails to distinguish the atomic energies for a given structures<sup>45,46</sup>. Therefore, Set #2 includes many structures with smaller unit cells to allow for better descriptions to the atomic energies. Hence, this can improve the performance in predicting the total energy of the structure. Lastly, Set #2 can be further extended to consist of more variety in atomic environments to enhance the capability of the current NNP.

*Descriptors.* As the complexity of a system's PES increases, different atomic descriptors can yield different accuracy in MLIAP development<sup>24</sup>. The key to extract reliable descriptors is by reconstructing the atomic neighbor density function. The expansion of bispectrum coefficients as the descriptor is more straightforward to be applied than the Gaussian symmetry functions. Nevertheless, it is important to take account of the relation between computational cost and accuracy in MLIAP training. The current MLIAP is developed through the reconstruction of neighbor density function, which is described by the Dirac  $\delta$  function. The full description of the true neighbor density can only be partially represented by finite spherical harmonics expansion. In addition, it is numerically unstable to compare the differences between



two  $\delta$  functions. A better design of descriptor uses smooth Gaussian functions to express the atomic neighbor density, as recently developed in SOAP method<sup>24</sup>. The comparison between SO(4) bispectrum and SOAP descriptors for NNP development will be conducted in the future code development. Moreover, other similar type of descriptors, such momentum tensor potential (MTP)<sup>14</sup>, will be investigated in the future.

*Fitting scheme.* Linear regression, as the simplest method in curve fitting, has been used in developing several MLIAPs<sup>11,14</sup>. In particular, the MTP approach<sup>19</sup> can predict energy and forces with great accuracy while maintaining acceptable computational cost. The advantage of linear regression method lies in its simple algorithm which provides easy and fast computation. Here we emphasize that by applying normalization to the descriptors can help improving the MLIAP training. However, linear regression can be sensitive to the noise in the data set. We also applied NN regression in this study. In general NN has more flexibility, which can yield better accuracy, in MLIAP fitting. However, overfitting often occurs in NN training. Our code considers regularization term in the loss function to prevent overfitting. Beside NN, some non-parametric regression techniques, such as Gaussian Process Regression, have also been proved to be efficient in MLIAP development<sup>16</sup>. However, this is beyond the scope of the current study.

*Applicability.* For the purpose of MD simulation around the equilibrium state, fitting the MLIAP with a localized data set generated from MD simulation is perhaps sufficient. However, the primary goal of this work is to generate high quality silicon MLIAP for the purpose of CSP, which requires a complete description of PES for a given chemical system. As discussed above, the MLIAP trained with the more diverse data set is generally capable of describing the entire PES better. We expect that the MLIAP generated in this work can be used to replace DFT simulation for predicting the structures of crystalline silicon, given that similar works have been done in several elemental systems<sup>22,23</sup>. Yet, one needs to keep in mind that the quality still depends on the coverage of training data set. For instance, additional data is needed to enable the prediction for surfaces and clusters<sup>26</sup>. Moreover, the trained MLIAP may not be able to describe the high energy configurations well, since Set #2 only contains structures with energy less than -4.0 eV/atom. It was found that some nonphysical configurations (e.g., short distances and overly clustered) may be favored under high temperature MD simulations. In this case, it is useful to add a few explicit two-body and three-

body terms to prevent the nonphysical configurations<sup>47</sup>. We will consider the combination of physical and machine learning terms in the training and investigate the applicability.

## V. CONCLUSIONS

In summary, we present a systematic investigation of MLFFs for elemental silicon using our in-house code. The silicon MLIAPs are developed by implementing different regression techniques based on Gaussian symmetry functions and bispectrum coefficients as the descriptors. The MLIAPs trained with Set #1 (the localized data set) can be described accurately in both energy and forces using generalized linear regression and NN based on both Gaussian symmetry functions and bispectrum coefficients. Among the MLIAPs, fitting NNP with the bispectrum coefficients is the most favorable option. This is due to the expansion of bispectrum coefficients is more straightforward than Gaussian symmetry functions. In addition, NNP provides more flexible framework in which the functional form can be easily adjusted by adding/reducing the size of weight parameters. However, Set #1 has poor transferability in predicting Set #2—the data set that provides more diversity of silicon. With Set #2, the NNP fitting with bispectrum coefficients achieves satisfactory accuracy at 13 meV/atom for energy and 0.08 eV/Å for force. In addition, Set #2 MLIAP can adequately describe Set #1. A more thorough study on the transferability of Set #2 silicon MLIAP and its comparison with other FF methods will be the main focus in future work. The source code and training data Set #2 are available at [https://github.com/qzhu2017/PyXtal\\_FF](https://github.com/qzhu2017/PyXtal_FF).

## VI. ACKNOWLEDGMENTS

We acknowledge the NSF (I-DIRSE-IL: 1940272) and NASA (80NSSC19M0152) for financial support. HY is also supported by the Science Graduate Student Research (SCGSR) program, which is administered by the Oak Ridge Institute for Science and Education (ORISE) for the DOE under contract number DE-SC0014664. The computing resources are provided by XSEDE (TG-DMR180040). A portion of this work was performed under the auspices of the U.S. Department of Energy by Lawrence Livermore National Laboratory under Contract DE-AC52-07NA27344.

---

\* [qiang.zhu@unlv.edu](mailto:qiang.zhu@unlv.edu)

<sup>1</sup> Kurt Lejaeghere, Gustav Bihlmayer, Torbjörn Björkman, Peter Blaha, Stefan Blügel, Volker Blum, Damien Caliste, Ivano E Castelli, Stewart J Clark, Andrea Dal Corso, et al. Reproducibility in density functional theory calculations of solids. *Science*, 351 (6280):aad3000, 2016. doi:10.1126/science.aad3000.

<sup>2</sup> Savas Berber, Young-Kyun Kwon, and David Tománek. Unusually high thermal conductivity of carbon nanotubes. *Phys. Rev. Lett.*, 84(20):4613, 2000. doi:10.1103/PhysRevLett.84.4613.

URL <https://doi.org/10.1103/PhysRevLett.84.4613>.

<sup>3</sup> Vesselin Yamakov, Dieter Wolf, Simon R Phillpot, Amiya K Mukherjee, and Herbert Gleiter. Dislocation processes in the deformation of nanocrystalline aluminium by molecular-dynamics simulation. *Nat. Mater.*, 1(1):45, 2002. doi:10.1038/nmat700. URL <https://doi.org/10.1038/nmat700>.

<sup>4</sup> V Yamakov, D Wolf, SR Phillpot, AK Mukherjee, and H Gleiter. Deformation-mechanism map for nanocrystalline metals by molecular-dynamics simulation. *Nat. Mater.*, 3(1):43, 2004. doi:

- 10.1038/nmat1035. URL <https://doi.org/10.1038/nmat1035>.
- <sup>5</sup> Artem R Oganov, Chris J Pickard, Qiang Zhu, and Richard J Needs. Structure prediction drives materials discovery. *Nat. Rev. Mater.*, 4:331348, 2019. ISSN 2058-8437. doi:10.1038/s41578-019-0101-8. URL <https://doi.org/10.1038/s41578-019-0101-8>.
- <sup>6</sup> Stefano Curtarolo, Gus LW Hart, Marco Buongiorno Nardelli, Natalio Mingo, Stefano Sanvito, and Ohad Levy. The high-throughput highway to computational materials design. *Nat. Mater.*, 12(3):191, 2013. doi:10.1038/nmat3568.
- <sup>7</sup> Albert P Bartók, Michael J Gillan, Frederick R Manby, and Gábor Csányi. Machine-learning approach for one-and two-body corrections to density functional theory: Applications to molecular and condensed water. *Phys. Rev. B*, 88(5):054104, 2013. doi:10.1103/PhysRevB.88.054104. URL <https://doi.org/10.1103/PhysRevB.88.054104>.
- <sup>8</sup> Nongnuch Artrith, Tobias Morawietz, and Jörg Behler. High-dimensional neural-network potentials for multicomponent systems: Applications to zinc oxide. *Phys. Rev. B*, 83(15):153101, 2011. doi:10.1103/PhysRevB.83.153101. URL <https://doi.org/10.1103/PhysRevB.83.153101>.
- <sup>9</sup> Rustam Z Khaliullin, Hagai Eshet, Thomas D Kühne, Jörg Behler, and Michele Parrinello. Nucleation mechanism for the direct graphite-to-diamond phase transition. *Nat. Mater.*, 10(9):693, 2011. doi:https://doi.org/10.1038/nmat3078. URL <https://doi.org/10.1038/nmat3078>.
- <sup>10</sup> Jörg Behler, Roman Martoňák, Davide Donadio, and Michele Parrinello. Metadynamics simulations of the high-pressure phases of silicon employing a high-dimensional neural network potential. *Phys. Rev. Lett.*, 100(18):185501, 2008. doi:10.1103/PhysRevLett.100.185501. URL <https://doi.org/10.1103/PhysRevLett.100.185501>.
- <sup>11</sup> Aidan P Thompson, Laura P Swiler, Christian R Trott, Stephen M Foiles, and Garritt J Tucker. Spectral neighbor analysis method for automated generation of quantum-accurate interatomic potentials. *J. Comput. Phys.*, 285:316–330, 2015. doi:10.1016/j.jcp.2014.12.018. URL <https://doi.org/10.1016/j.jcp.2014.12.018>.
- <sup>12</sup> Mitchell A Wood and Aidan P Thompson. Extending the accuracy of the snap interatomic potential form. *J. Chem. Phys.*, 148(24):241721, 2018. doi:10.1063/1.5017641. URL <https://doi.org/10.1063/1.5017641>.
- <sup>13</sup> Sergey Pozdnyakov, Artem R. Oganov, Arslan Mazitov, Timofey Frolov, Ivan Kruglov, and Efim Mazhnik. Fast general two- and three-body interatomic potential, 2019.
- <sup>14</sup> Alexander V. Shapeev. Moment tensor potentials: A class of systematically improvable interatomic potentials. *Multiscale Model. Simul.*, 14(3):1153–1173, 2016. doi:10.1137/15M1054183. URL <https://doi.org/10.1137/15M1054183>.
- <sup>15</sup> Albert P Bartók, Mike C Payne, Risi Kondor, and Gábor Csányi. Gaussian approximation potentials: The accuracy of quantum mechanics, without the electrons. *Phys. Rev. Lett.*, 104(13):136403, 2010. doi:10.1103/PhysRevLett.104.136403. URL <https://doi.org/10.1103/PhysRevLett.104.136403>.
- <sup>16</sup> Albert P Bartók and Gábor Csányi. Gaussian approximation potentials: A brief tutorial introduction. *Int. J. Quantum Chem.*, 115(16):1051–1057, 2015. doi:10.1002/qua.24927. URL <https://doi.org/10.1002/qua.24927>.
- <sup>17</sup> Jörg Behler and Michele Parrinello. Generalized neural-network representation of high-dimensional potential-energy surfaces. *Phys. Rev. Lett.*, 98(14):146401, 2007. doi:10.1103/PhysRevLett.98.146401. URL <https://doi.org/10.1103/PhysRevLett.98.146401>.
- <sup>18</sup> Jörg Behler. Constructing high-dimensional neural network potentials: A tutorial review. *Int. J. Quantum Chem.*, 115(16):1032–1050, 2015. doi:10.1002/qua.24890. URL <https://doi.org/10.1002/qua.24890>.
- <sup>19</sup> Yunxing Zuo, Chi Chen, Xiangguo Li, Zhi Deng, Yiming Chen, Jörg Behler, Gábor Csányi, Alexander V Shapeev, Aidan P Thompson, Mitchell A Wood, et al. A performance and cost assessment of machine learning interatomic potentials. *arXiv preprint arXiv:1906.08888*, 2019. URL <https://arxiv.org/abs/1906.08888>.
- <sup>20</sup> Samad Hajinazar, Junping Shao, and Aleksey N. Kolmogorov. Stratified construction of neural network based interatomic models for multicomponent materials. *Phys. Rev. B*, 95:014114, Jan 2017. doi:10.1103/PhysRevB.95.014114. URL <https://link.aps.org/doi/10.1103/PhysRevB.95.014114>.
- <sup>21</sup> T. L. Jacobsen, M. S. Jørgensen, and B. Hammer. On-the-fly machine learning of atomic potential in density functional theory structure optimization. *Phys. Rev. Lett.*, 120:026102, Jan 2018. doi:10.1103/PhysRevLett.120.026102. URL <https://link.aps.org/doi/10.1103/PhysRevLett.120.026102>.
- <sup>22</sup> Volker L Deringer, Chris J Pickard, and Gábor Csányi. Data-driven learning of total and local energies in elemental boron. *Phys. Rev. Lett.*, 120(15):156001, 2018. doi:10.1103/PhysRevLett.120.156001. URL <https://doi.org/10.1103/PhysRevLett.120.156001>.
- <sup>23</sup> Evgeny V Podryabinkin, Evgeny V Tikhonov, Alexander V Shapeev, and Artem R Oganov. Accelerating crystal structure prediction by machine-learning interatomic potentials with active learning. *Phys. Rev. B*, 99(6):064114, 2019. doi:10.1103/PhysRevB.99.064114. URL <https://doi.org/10.1103/PhysRevB.99.064114>.
- <sup>24</sup> Albert P. Bartók, Risi Kondor, and Gábor Csányi. On representing chemical environments. *Phys. Rev. B*, 87:184115, May 2013. doi:10.1103/PhysRevB.87.184115. URL <https://link.aps.org/doi/10.1103/PhysRevB.87.184115>.
- <sup>25</sup> Zhenwei Li, James R. Kermode, and Alessandro De Vita. Molecular dynamics with on-the-fly machine learning of quantum-mechanical forces. *Phys. Rev. Lett.*, 114:096405, Mar 2015. doi:10.1103/PhysRevLett.114.096405. URL <https://link.aps.org/doi/10.1103/PhysRevLett.114.096405>.
- <sup>26</sup> Albert P. Bartók, James Kermode, Noam Bernstein, and Gábor Csányi. Machine learning a general-purpose interatomic potential for silicon. *Phys. Rev. X*, 8:041048, Dec 2018. doi:10.1103/PhysRevX.8.041048. URL <https://link.aps.org/doi/10.1103/PhysRevX.8.041048>.
- <sup>27</sup> Hasan Babaei, Ruiqiang Guo, Amirreza Hashemi, and Sangyeop Lee. Machine-learning-based interatomic potential for phonon transport in perfect crystalline si and crystalline si with vacancies. *Phys. Rev. Materials*, 3:074603, Jul 2019. doi:10.1103/PhysRevMaterials.3.074603. URL <https://link.aps.org/doi/10.1103/PhysRevMaterials.3.074603>.
- <sup>28</sup> Luigi Bonati and Michele Parrinello. Silicon liquid structure and crystal nucleation from ab initio deep metadynamics. *Phys. Rev. Lett.*, 121:265701, Dec 2018. doi:10.1103/PhysRevLett.121.265701. URL <https://link.aps.org/doi/10.1103/PhysRevLett.121.265701>.
- <sup>29</sup> Scott Fredericks, Dean Sayre, and Qiang Zhu. Pyxtal: a python library for crystal structure generation and symmetry analysis. 2019.
- <sup>30</sup> Ask Hjørth Larsen, Jens Jørgen Mortensen, Jakob Blomqvist, Ivano E Castelli, Rune Christensen, Marcin Dułak, Jesper Friis, Michael N Groves, Bjørk Hammer, Cory Hargus, et al. The atomic simulation environment a python library for working with atoms. *J. Phys. Condensed Matter*, 29(27):273002, 2017. doi:10.1088/1361-648X/aa680e. URL <https://doi.org/10.1088/1361-648X/aa680e>.

- <sup>31</sup> Georg Kresse and Jürgen Furthmüller. Efficient iterative schemes for ab initio total-energy calculations using a plane-wave basis set. *Phys. Rev. B*, 54(16):11169, 1996. doi: 10.1103/PhysRevB.54.11169. URL <https://doi.org/10.1103/PhysRevB.54.11169>.
- <sup>32</sup> Peter E Blöchl. Projector augmented-wave method. *Phys. Rev. B*, 50(24):17953, 1994. doi:10.1103/PhysRevB.50.17953. URL <https://doi.org/10.1103/PhysRevB.50.17953>.
- <sup>33</sup> John P. Perdew, Kieron Burke, and Matthias Ernzerhof. Generalized gradient approximation made simple. *Phys. Rev. Lett.*, 77:3865–3868, 1996. doi:10.1103/PhysRevLett.77.3865. URL <https://doi.org/10.1103/PhysRevLett.77.3865>.
- <sup>34</sup> M. Gastegger, L. Schwiedrzik, M. Bittermann, F. Berzsényi, and P. Marquetand. wacsf weighted atom-centered symmetry functions as descriptors in machine learning potentials. *J. Chem. Phys.*, 148(24):241709, 2018. doi:10.1063/1.5019667. URL <https://doi.org/10.1063/1.5019667>.
- <sup>35</sup> Giulio Imbalzano, Andrea Anelli, Daniele Giofre, Sinja Klees, Jorg Behler, and Michele Ceriotti. Automatic selection of atomic fingerprints and reference configurations for machine-learning potentials. *J. Chem. Phys.*, 148(24):241730, 2018. doi: 10.1063/1.5024611. URL <https://doi.org/10.1063/1.5024611>.
- <sup>36</sup> Tran Doan Huan, Rohit Batra, James Chapman, Sridevi Krishnan, Lihua Chen, and Rampi Ramprasad. A universal strategy for the creation of machine learning-based atomistic force fields. *npj Comput. Mater.*, 3, 2017. doi:10.1038/s41524-017-0042-y. URL <https://doi.org/10.1038/s41524-017-0042-y>.
- <sup>37</sup> Hao Gao, Junjie Wang, and Jian Sun. Improve the performance of machine-learning potentials by optimizing descriptors. *J. Chem. Phys.*, 150(24):244110, 2019. doi:10.1063/1.5097293. URL <https://doi.org/10.1063/1.5097293>.
- <sup>38</sup> Steve Plimpton. Fast parallel algorithms for short-range molecular dynamics. *J. Comp. Phys.*, 117(1):1 – 19, 1995. ISSN 0021-9991. doi:https://doi.org/10.1006/jcph.1995.1039.
- <sup>39</sup> Michael Boyle. Angular velocity of gravitational radiation from precessing binaries and the corotating frame. *Phys. Rev. D*, 87: 104006, May 2013. doi:10.1103/PhysRevD.87.104006. URL <https://link.aps.org/doi/10.1103/PhysRevD.87.104006>.
- <sup>40</sup> Travis E Oliphant. *A guide to NumPy*, volume 1. Trelgol Publishing USA, 2006. URL <http://www.numpy.org/>.
- <sup>41</sup> Diederik P. Kingma and Jimmy Ba. Adam: A method for stochastic optimization, 2014. URL <http://arxiv.org/abs/1412.6980>. Published as a conference paper at the 3rd International Conference for Learning Representations, San Diego, 2015.
- <sup>42</sup> Pauli Virtanen, Ralf Gommers, Travis E. Oliphant, Matt Haberland, Tyler Reddy, David Cournapeau, Evgeni Burovski, Pearu Peterson, Warren Weckesser, Jonathan Bright, Stéfan J. van der Walt, Matthew Brett, Joshua Wilson, K. Jarrod Millman, Nikolay Mayorov, Andrew R. J. Nelson, Eric Jones, Robert Kern, Eric Larson, CJ Carey, İlhan Polat, Yu Feng, Eric W. Moore, Jake VanderPlas, Denis Laxalde, Josef Perktold, Robert Cimrman, Ian Henriksen, E. A. Quintero, Charles R Harris, Anne M. Archibald, Antônio H. Ribeiro, Fabian Pedregosa, Paul van Mulbregt, and SciPy 1.0 Contributors. SciPy 1.0—Fundamental Algorithms for Scientific Computing in Python. *arXiv e-prints*, page arXiv:1907.10121, 2019. URL <https://arxiv.org/abs/1907.10121>.
- <sup>43</sup> Ciyu Zhu, Richard H. Byrd, Peihuang Lu, and Jorge Nocedal. Algorithm 778: L-bfgs-b: Fortran subroutines for large-scale bound-constrained optimization. *ACM Trans. Math. Softw.*, 23(4):550–560, December 1997. ISSN 0098-3500. doi:10.1145/279232.279236. URL <http://doi.acm.org/10.1145/279232.279236>.
- <sup>44</sup> Andriy O Lyakhov, Artem R Oganov, Harold T Stokes, and Qiang Zhu. New developments in evolutionary structure prediction algorithm uspeX. *Comput. Phys. Commun.*, 184(4):1172–1182, 2013. doi:10.1016/j.cpc.2012.12.009.
- <sup>45</sup> Yufeng Huang, Jun Kang, William A. Goddard, and Lin-Wang Wang. Density functional theory based neural network force fields from energy decompositions. *Phys. Rev. B*, 99:064103, Feb 2019. doi:10.1103/PhysRevB.99.064103. URL <https://link.aps.org/doi/10.1103/PhysRevB.99.064103>.
- <sup>46</sup> Dongsun Yoo, Kyuhyun Lee, Wonseok Jeong, Dongheon Lee, Satoshi Watanabe, and Seungwu Han. Atomic energy mapping of neural network potential. *Phys. Rev. Mater.*, 3:093802, Sep 2019. doi:10.1103/PhysRevMaterials.3.093802. URL <https://link.aps.org/doi/10.1103/PhysRevMaterials.3.093802>.
- <sup>47</sup> Volker L. Deringer and Gábor Csányi. Machine learning based interatomic potential for amorphous carbon. *Phys. Rev. B*, 95: 094203, Mar 2017. doi:10.1103/PhysRevB.95.094203. URL <https://link.aps.org/doi/10.1103/PhysRevB.95.094203>.